
Direct-Drive Cryogenic Target Implosion Performance on OMEGA

Introduction

Direct-drive, cryogenic inertial confinement fusion (ICF) capsule implosion experiments under investigation using the 30-kJ OMEGA laser system¹ at LLE will validate the scaled-ignition performance of low-adiabat, cryogenic DT capsules. This validation is pivotal in the development of direct-drive ignition target designs for the 1.6-MJ National Ignition Facility² (NIF), currently under construction at the Lawrence Livermore National Laboratory. The physical limitations of the target fabrication and laser subsystems on the NIF, however, place restrictions on the robustness of ICF ignition designs. Demonstrating the viability of the ignition designs driven under a variety of perturbation scenarios is critical to the success of direct-drive ICF.

Target designers have, in the past, had to trade target performance (thermonuclear gain) for increased target stability.³ Many studies have been undertaken to examine the minimum laser energy required to achieve ignition.^{4–7} All of these studies have concluded that the minimum energy required for ignition scales as $\sim\alpha^2$, where α is the shell adiabat, defined as the ratio of the local pressure to the Fermi-degenerate pressure. As the compressibility of the fuel is increased (α decreased), less laser energy is required to achieve ignition; however, more-compressible fuel develops thinner fuel layers during the implosion, resulting in reduced stability and, potentially, layer failure. As the nonuniformity levels are reduced, it becomes possible to field targets with lower fuel adiabat, examining regions of higher target gain for fixed laser energy. Eventually, targets with a fuel adiabat approaching $\alpha = 1$ will be used in direct-drive ignition.

The cryogenic implosion campaign at LLE is a staged program comprised of several concurrent efforts including experimental validation of target performance for progressively lower fuel adiabat target designs employing cryogenic D₂ fuel; physical minimization of the interfacial cryogenic surface roughness; and ultimately the implosion of cryogenic DT targets on the OMEGA laser system. Recent advances in all three of these efforts have LLE poised to demonstrate

scaled-ignition performance with DT on OMEGA by the end of FY05. Significant progress has been made in cryogenic implosion experiments evaluating target performance with high-adiabat solid-D₂ and wetted-foam targets and low-adiabat solid-D₂ targets. It has been shown that there is good agreement between the experimental observables and the results of two-dimensional *DRACO*⁸ simulations for targets imploded near target chamber center (TCC). The use of adiabat shaping⁹ has been shown theoretically to lead to increased stability for both the “all-DT” and wetted-foam direct-drive NIF point designs and the corresponding ignition-scaled experiments for OMEGA. Dramatic advances in cryogenic layer characterization and layering over the last year have resulted in the production of sub-2- μm inner surface ice layers in targets for implosion on OMEGA. The cryogenic DT fill and transfer station (FTS) is currently being qualified and will be DT-charged by the end of this fiscal year. With this system in place, full-scale layering studies of cryogenic DT targets will be undertaken, resulting in the fielding of ignition-scale cryogenic DT experiments on OMEGA.

This article reviews the performance characteristics of recent OMEGA cryogenic implosion experiments and outlines the theoretical basis for new cryogenic experiments that will examine low, $\alpha = 2$ implosions for OMEGA. In the following sections, (1) the experimental setup is presented; (2) results of the implosion experiments are compared with results from one- and two-dimensional (1-D, 2-D) radiation-hydrodynamics simulations; (3) the direct-drive ignition design is optimized for better hydrodynamic stability using a picket prepulse; and (4) the scaling of this design to OMEGA operating conditions is examined. Conclusions are presented in the last section.

Experimental Setup

1. Laser-System Configuration

Cryogenic capsules were imploded using two pulse shapes: a high-adiabat ($\alpha \sim 25$), 23-kJ, 1-ns square pulse and a low-adiabat ($\alpha \sim 4$), 17-kJ, 2.5-ns shaped pulse. The $\alpha \sim 4$ pulse shape has been scaled from the standard all-DT as shown in

Fig. 97.1. Full beam smoothing techniques were applied to each pulse using distributed phase plates (DPP's),¹⁰ polarization smoothing with distributed polarization rotators (DPR's),¹¹ and 2-D, single-color-cycle, 1-THz smoothing by spectral dispersion (SSD).¹² Laser power balance was optimized using techniques employing x-ray fluence measurements of standard OMEGA pointing targets.¹³ With these techniques the variance of incident energy imbalance among all 60 OMEGA beams is $\sim 2\%$ rms, with a 4- to 5-ps rms mistiming when taken to target.

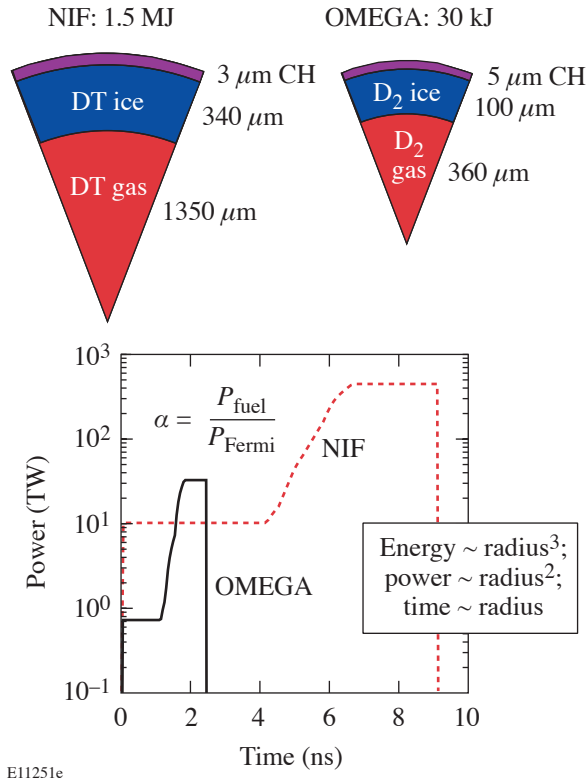


Figure 97.1
The direct-drive NIF point design target is shown with the corresponding OMEGA $\alpha = 4$, energy-scaled capsule. The scaled pulse shapes are given in the inset.

2. Capsule Metrology and Layering

Capsules used in these experiments fell into one of two categories: utilizing fuel layers comprised of either solid D_2 (SD) or a D_2 wetted-foam (WF) layer over a solid D_2 layer. The SD target employs a thin, plastic outer shell composed of a “strong GDP” (glow discharge polymer) (a high-strength plastic, $CH_{1.1}$ $\rho \sim 1.20$ g/cc) approximately $4 \mu\text{m}$ thick. This shell, nominally $850 \mu\text{m}$ in diameter, is permeation filled with

D_2 to pressures at room temperature in excess of 1000 atm, which, when properly cooled, forms an ice layer of approximately $100 \mu\text{m}$. Layering this surface requires the proper selection of the triple-point isotherm in the capsule, cooling gas pressure, and IR heating laser energy input. Currently a quality layer ($< 2 \mu\text{m}$ rms) requires several days of technician time. Optimization of this effort is being studied. Layer roughness for this study spanned a range of values from 2 to $7 \mu\text{m}$ rms.

The WF shell used in these experiments was not optimized for implosion on OMEGA but was part of initial foam-ice layering studies in collaboration with General Atomics. The shell consisted of a $4\text{-}\mu\text{m}$ CH layer overcoating a $62\text{-}\mu\text{m}$ foam shell. The foam had a dry density of 120 mg/cc, with fibers consisting of the same GDP mentioned above and an average cell size of less than $1 \mu\text{m}$. This shell underwent the same permeation fueling as the standard SD cryogenic target, which resulted in an inner ice layer estimated to be $65 \mu\text{m}$ in depth. Accurate knowledge of the wetted-foam density and the resultant ice-layer thickness depends on the modeling of the freezing of the liquid D_2 fuel within the foam matrix. For this experiment it was assumed that the foam, as it was cooled, became impermeable to the liquid D_2 , preventing any diffusion of liquid D_2 in or out of the foam matrix. Conserving mass, the wetted-foam density remains constant (~ 240 mg/cc) as densification proceeds.

While characterization of WF targets remains an issue due to significant diffraction of the incident probe light, the SD targets are characterized with white-light shadowgraphy similar to that first proposed and implemented by Koch.¹⁴ The shadowgraphy technique produces a wealth of experimental signal represented by a series of rings in the target image plane. Recent analysis¹⁵ has identified the source of the faint trace rings and confirmed the validity of the “bright ring” as the primary carrier of information about the interfacial ice roughness. After processing the information for a particular target orientation, the target is rotated about its polar axis and another sample is taken and processed. Such information can then be interpolated and processed to give a full, 3-D representation of the inner ice surface. The number of experimentally obtained traces, as was pointed out by Stephens,¹⁶ limits the spatial scale of this representation. OMEGA capsules undergo a minimum of 20 roughness scans, which describe the amplitude and nature of the first ten spherical harmonics. Complete spectral decomposition of the ice surface would require more than a hundred angular samples.

3. Target Positioning

Sangster¹⁷ reported the early problems with positioning cryogenic targets in the center of the OMEGA target chamber. At the heart of this problem was static mis-positioning due to image distortion through the shroud windows and dynamic mis-positioning due to target vibration. The static mis-positioning was corrected with careful and detailed procedures comparing and documenting the position of surrogate targets as viewed through the shroud windows and their true position after the shroud was retracted. Each of the four moving cryogenic transfer carts (MCTC's) was examined and given a unique set of positioning reticules for use with target experiments.

The target vibration was caused by two problems: (1) the vibration induced to the target stalk as the cryogenic shroud, used to maintain the correct environment for the ice layer, was pulled away from the target before laser irradiation, and (2) an occasional, weak collision between the articulated target stalk and the cryogenic shroud during this retraction. Many engineering improvements were applied to the target shroud and the MCTC. The most effective of these included the modification to the shroud control software allowing a slower retraction of the shroud and the replacement of the articulated target stalks with a simple, narrower staple design. The slower retraction speed allows transmitted vibrations to self-damp, while the narrower stalk reduces the possibility of a collision between the target and the retracting shroud.

With these modifications in place, the static mis-pointing has now been reduced to less than $40\ \mu\text{m}$ for all of the MCTC's, while target vibration has been virtually eliminated. All target implosions discussed in this article were located within $40\ \mu\text{m}$ of TCC, with many achieving $20\ \mu\text{m}$ at shot time.

4. Diagnostics

Cryogenic implosions on the OMEGA laser system are diagnosed with a large number of instruments, including laser scattering and absorption diagnostics; time-dependent and time-integrated x-ray imaging; time-dependent and time-integrated x-ray spectroscopy; time-dependent and time-integrated fusion yield measurement; and fusion product spectroscopy. The fusion product diagnostics include measurements of both neutrons and charged particles. Data presented here include measurements from the time-integrated x-ray imaging, primary¹⁸ and secondary fusion yield,¹⁹ neutron²⁰ and proton spectroscopy,²¹ and time-dependent neutron and proton emission.²²

Time-integrated x-ray imaging is used to determine the position of the target at the time of the shot. These measurements are made with both x-ray pinhole cameras and x-ray microscopes. Three x-ray microscopes and five x-ray pinhole cameras located in fixed positions around the target chamber allow several views of the target emission to be recorded. Subsequent analysis of the images locates the position of the target to within $\pm 10\ \mu\text{m}$.

The primary and secondary fusion product yields are measured with a combination of activation, scintillation, and track detectors. These provide a direct measure of the implosion performance. The ratio of secondary to primary product yields is a measure of the final core conditions. Neutron spectroscopy is used to determine the ion temperature, and the proton spectroscopy determines the total areal density of the implosion from the energy loss measured by wedged range filters.²³

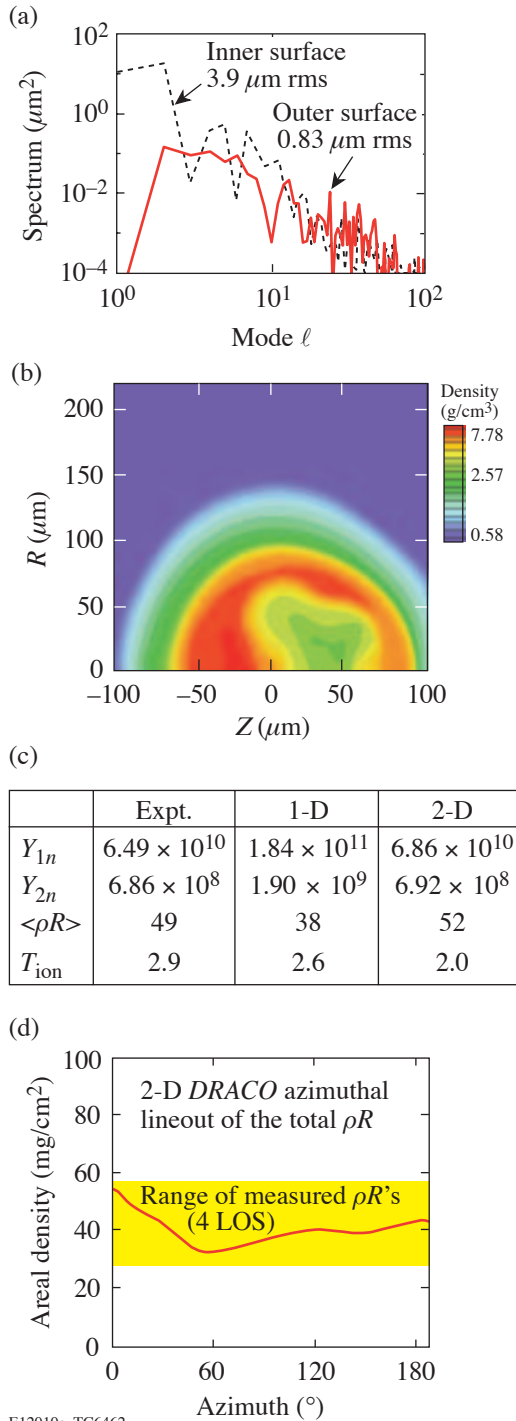
Time-dependent neutron emission is measured with a scintillator coupled to an optical streak camera. The time evolution of the fusion emission is sensitive to the overall coupling of the laser energy to the target, and the emission from both the shock wave and compression can be observed. These data and those taken from laser absorption measurements are used to determine the accuracy of the hydrodynamic simulation of the implosion.

Implosion Results

1. High-Adiabatic Pulses

The cryogenic implosion campaign is divided into several phases dealing with the validation of stable implosions with progressively lower fuel adiabat. The first phase of these implosions used a high-adiabat (1-ns square, $\alpha = 25$) laser pulse to minimize the effects of laser imprint on target performance. This allows experimental investigation of the effect of ice roughness on target performance. Implosions were carried out using several SD targets and one WF target. For brevity we will examine one SD shot in detail and then speak briefly about the wetted-foam shot.

The SD capsule used was $\sim 875\ \mu\text{m}$ in diameter and contained a $92\text{-}\mu\text{m}$ D_2 -ice layer surrounded by a $3.8\text{-}\mu\text{m}$ GDP wall. The inner ice roughness was measured to be $\sim 4\ \mu\text{m}$ rms when averaged over 23 views. The power spectrum, shown in Fig. 97.2(a), is heavily weighted toward the lowest end of the spectrum with $\sim 90\%$ of the power contained in the first few modes ($\ell = 1$ to 3). The capsule was determined experimentally¹³ to be offset $22\ \mu\text{m}$ from target chamber center at the



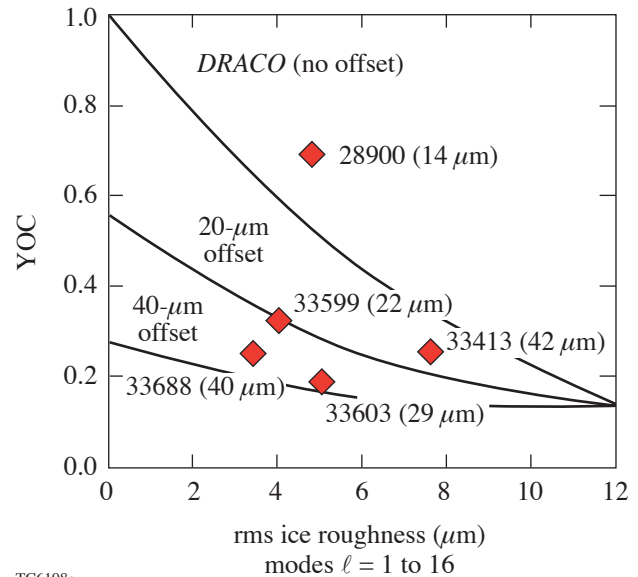
E12010e, TC6462

Figure 97.2

Two-dimensional *DRACO* input and results for shot 33599. (a) Input ice roughness spectrum, (b) isodensity contours drawn near the time of peak burn, (c) tabular comparison of secondary-neutron yields and neutron-averaged areal density and ion temperature, and (d) angular variation of the total areal density calculated from the isodensity contours. Yellow region represents the range of experimentally obtained areal-density measurements.

beginning of the implosion. This capsule produced a neutron yield of 6.5×10^{10} neutrons—roughly 36% of the simulated 1-D *LILAC*²⁴ yield. A *DRACO* simulation was run with the roughness spectra from Fig. 97.2(a) and an initial 4.4% rms $\ell = 1$ illumination nonuniformity corresponding to the 22- μm offset.¹³ The simulated neutron yield of 6.9×10^{10} falls very close to the experimental result. As can be seen from the isodensity contours given in Fig. 97.2(b) (taken near the time of peak neutron production), the core has developed under the strong influence of the low modes with the effect of the $\ell = 1$ and 2 most prominent. The secondary-proton yields and average-areal-density results, shown in Fig. 97.2(c), are also in good agreement between the experiment and the *DRACO* simulation. One of the more-interesting results from this implosion is the agreement between the range of experimentally observed areal-density measurements with those predicted by *DRACO* as shown in Fig. 97.2(d).

Additional results obtained for the other shots are compiled in Fig. 97.3. In Fig. 97.3 the experimental yield-over-clean [(YOC), the experimentally obtained yield divided by the 1-D simulated yield] for all shots in this series is compared with the trends of several series of perturbed *DRACO* simulations run with increasing initial ice roughness for a specific fixed target offset. The *DRACO* trend lines merge with increasing ice



TC6108a

Figure 97.3

Analysis of experimental neutron YOC drawn as a function of the target's initial ice roughness. Curves are drawn for several series of *DRACO* runs analyzing the degradation of YOC with increasing ice roughness. Each of these series was computed with a different initial target offset.

roughness due to the dominance of the ice perturbation at these high levels. The experimental results are in good agreement with the *DRACO* predictions.

The other part of the high-adiabat cryogenic implosion series was the use of a WF target to measure the absorption fraction and shock speed in this material. Such experiments, carried out in spherical geometry, help to develop a predictive capability for target performance. The need for examining shock propagation within a wetted-foam matrix was pointed out earlier^{25,26} in theoretical studies analyzing shock propagation in foam. Studies at LLE use the 2-D astrophysical code AMRCLAW²⁷ that employs the adaptive-mesh-refinement (AMR) scheme to highly resolve the shock flow around and through the fiber elements. The results of such simulations are shown in Fig. 97.4 and indicate that shocks travel faster in wetted foam when compared to traditional Lagrangian hydrodynamics simulations that model the foam as a homogeneous mixture. Of particular interest to target designers, in addition to ascertaining the proper value of the shock velocity, are the perturbed nature of the shock front and mechanisms for the CH-DT homogeneous annealing in the wake of the shock. Both of these processes will be examined in more detail when a new three-dimensional (3-D) AMR code, ASTROBEAR,²⁷ becomes available.

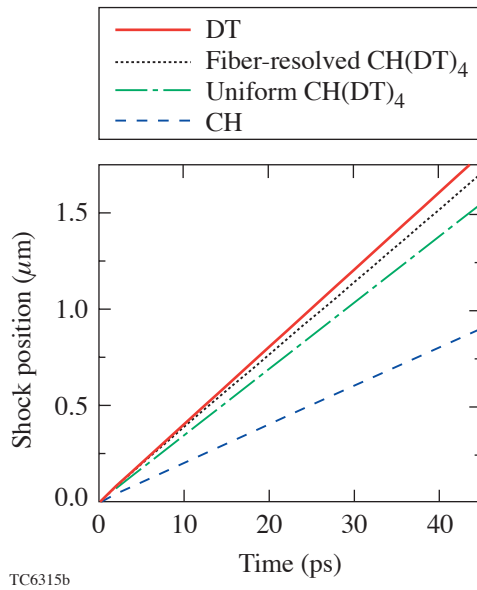


Figure 97.4 Numerical results detailing the difference in shock velocity for a variety of materials including CH, CH(DT)₄ mixture, fiber-resolved foam, and pure DT.

The first cryogenic wetted-foam implosion on OMEGA produced the highest-ever cryogenic neutron yield: 1.8×10^{11} . The target was imploded with the high-adiabat, 1-ns square pulse. The neutron burn history was obtained and is shown as the solid curve in Fig. 97.5. Several 1-D *LILAC* simulations were run with varying the wetted-foam density, and an example of the numerical burn history ($\rho_{WF} \sim 240$ mg/cc) is drawn as the dotted line in Fig. 97.5. Discrepancies between the simulated and experimental bang times may be attributed to lower shock velocities in low-density foams when modeled as a homogeneous mixture (as predicted in Refs. 25 and 26). The numerically obtained 1-D yield underestimates the experimental yield by roughly 15%.

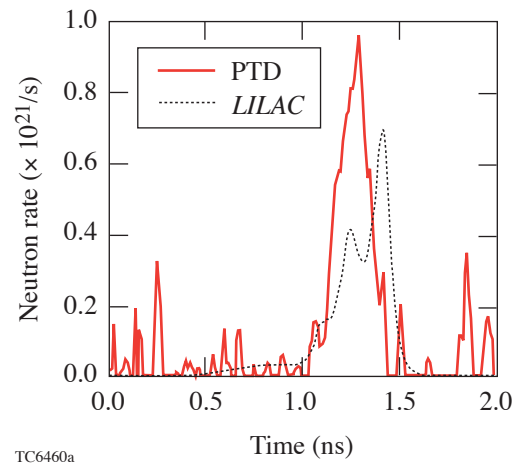


Figure 97.5 Comparison of neutron burn histories between the results of the particle temporal diagnostic (PTD) and *LILAC*.

Clearly, more work needs to be done in addressing the use of WF targets in ICF ignition experiments. Over the coming year we will repeat the spherical experiments for various density dry foams and couple this information with ongoing planar foam experiments studying shock transit with picket pulses in warm foams and standard shock development in cryogenic wetted foams. Additionally, techniques must be developed to characterize the ice layer within the foam shell.

2. Low-Adiabat Pulses

The next phase of the OMEGA cryogenic implosion program involves the validation of low-adiabat, ignition-scaled implosions on OMEGA. The first set of experiments in this phase employs the $\alpha = 4$ pulse shape, shown earlier in Fig. 97.1. Several implosions were undertaken using the

OMEGA laser, but, again, only a single SD shot will be described in detail.

The SD target was 865 μm in diameter with a 3.8-mm GDP overcoat, an ice layer of $\sim 92\text{-}\mu\text{m}$ depth, and an interior ice surface roughness of $\sim 4.5\ \mu\text{m}$. The power spectrum for this surface, as shown in Fig. 97.6(a), is again heavily weighted toward low-order modes. The capsule was determined to be 28 μm from target chamber center at the beginning of the implosion. The neutron yield for this implosion was 4.3×10^9 , which represents the highest-ever experimental yield obtained from a cryogenic $\alpha \sim 4$ implosion (YOC $\sim 16\%$). The spectra from Fig. 97.6(a) and an initial 5.6% $\ell = 1$ illumination nonuniformity, again due to the target offset, were used in a *DRACO* simulation (laser imprint was excluded from this calculation because the growth of these two perturbations, at these levels, overwhelms the effect of the imprint as was demonstrated in Ref. 3). The simulated yield was 5.9×10^9 . The secondary-yield comparison also showed the *DRACO* simulation slightly overpredicting the experimental result; however, the simulated average $\langle \rho R \rangle$ was again in good agreement as shown in Fig. 97.6(c) and the azimuthal variation in Fig. 97.6(d).

Previously,³ low-adiabat target performance has been presented as a compilation of all perturbation sources using a sum-in-quadrature representation of each source's contribution to the roughness of the inner ice layer at the end of the acceleration phase of the implosion. The scaling parameter $\bar{\sigma}$ is defined as

$$\bar{\sigma}^2 = 0.06 \times \sigma_\ell^2 (\ell < 10) + \sigma_\ell^2 (\ell \geq 10),$$

where σ_ℓ is the rms roughness computed over the mode range indicated. At this time during the implosion, this surface decouples from the ablation region of the target. As such, the effects of all major sources of perturbation leading to the initial seed of the deceleration-phase Rayleigh–Taylor (RT) instability have been set. An example of the $\bar{\sigma}$ scaling is shown in Fig. 97.7, where a comparison is made between the NIF $\alpha = 3$ and OMEGA $\alpha = 4$ designs.

Using the $\bar{\sigma}$ scaling with yield allows the experimental validation of the numerical modeling of current OMEGA experiments, which, in turn, lends credibility to the ability of these numerical models to predict ignition for direct-drive target designs on the NIF. The $\bar{\sigma}$ parameter and yield performance were extracted from the *DRACO* simulations of the

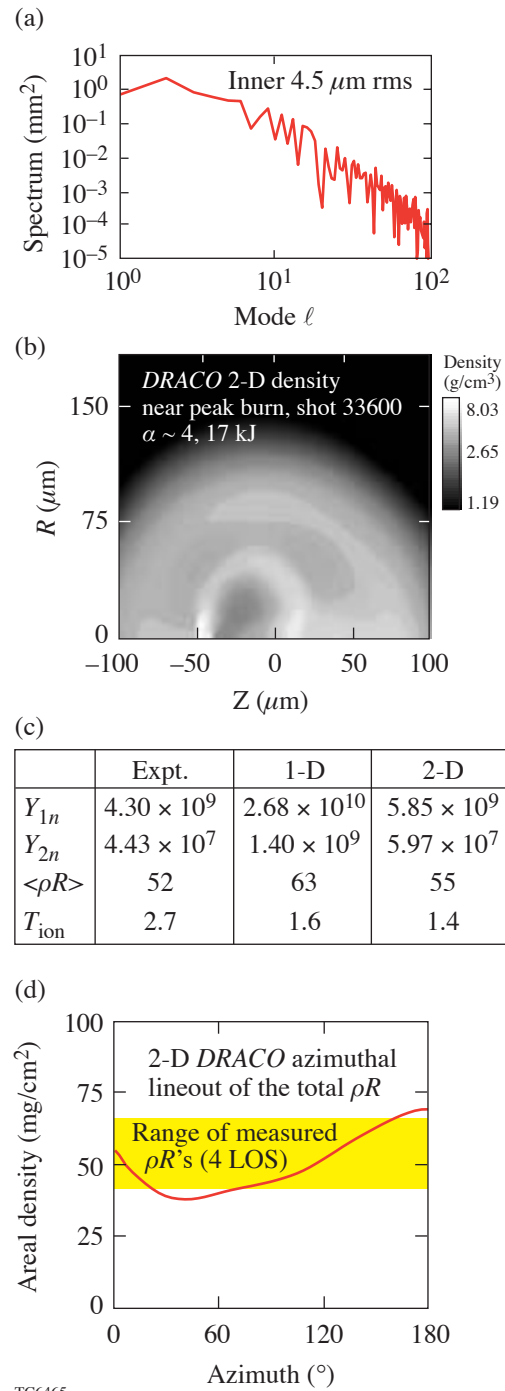


Figure 97.6

Two-dimensional *DRACO* input and results for shot 33600. (a) Input ice roughness spectrum, (b) isodensity contours drawn near the time of peak burn, (c) tabular comparison of secondary-neutron yields and neutron-averaged areal density and ion temperature, and (d) angular variation of the total areal density calculated from the isodensity contours. Yellow region represents the range of experimentally obtained areal-density measurements.

$\alpha = 4$ implosion experiments and placed on the graph in Fig. 97.7. It can be seen that the points are in reasonable agreement with the $\bar{\sigma}$ scaling. When nonuniformities on OMEGA are improved, implosion experiments will approach the $\sim 40\%$ YOQ goal for these implosions as denoted by the dashed lines in Fig. 97.7.

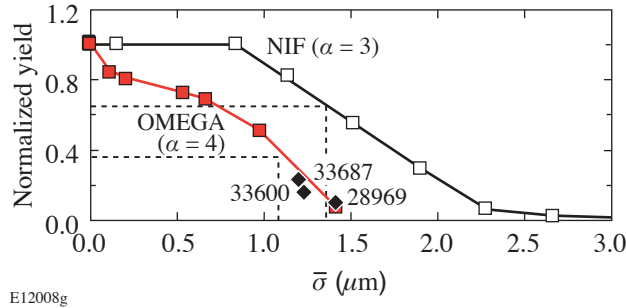


Figure 97.7 Comparison of the $\bar{\sigma}$ stability analysis for the NIF $\alpha = 3$ and the OMEGA $\alpha = 4$ designs. The dashed lines indicate the predicted value of $\bar{\sigma}$ and the corresponding target performance for each of the two designs when all NIF specifications for levels of nonuniformity are applied. The solid diamonds represent results from 2-D *DRACO* simulations of the noted OMEGA experiments.

Re-baseline of the Direct-Drive Point Design

The baseline direct-drive point design has not experienced any significant changes since its introduction by Verdon²⁸ in the early 1990s. The design, consisting of a levitated 340- μm -thick cryogenic DT layer coated with 3 μm of CH and irradiated with 1.8 MJ of 351-nm light, has undergone several design studies^{3,29,30} and has consistently been shown to be robust to moderate levels of perturbation. The design's only weakness, which can be attributed to low ablation velocities, is its strong susceptibility to laser imprint during the acceleration phase of the implosion. The limited ablation velocities cannot effectively stabilize the RT growth of the fast-growing, short-wavelength-laser nonuniformities present in the laser-beam profile. While several schemes have been adopted to smooth these nonuniformities,^{10–12} the maximum ratio of the perturbation amplitude to the in-flight shell thickness has been shown to approach 70% during the acceleration phase of the implosion.³¹

Recently, an old idea of modifying the seeds of RT growth within the ablation region using picket pulses³² has been examined for the point design.³³ Goncharov⁹ modified this process by employing a very narrow Gaussian picket added to the foot of the drive pulse to launch an early, unsupported shock

wave into the target. Because the shock wave is unsupported, it begins to decay after the rarefaction wave from the front surface (created at the end of the picket) catches up to it. As the shock decays, it creates a shaped adiabat within the fuel layer—low near the shock front and high near the ablation region. The high adiabat in the ablation region results in much higher ablation velocities, which, in turn, provide for increased stabilization of the RT growth present there.

The decaying shock technique has recently been applied to several direct-drive, high-gain target designs,^{34–36} including the Verdon point design. In all cases the scheme has been shown to dramatically reduce the deleterious effects of laser imprint. As such, the direct-drive-ignition design has been modified to include a 200-ps laser picket, and an energy-scaled design has been set for implosion experiments on OMEGA. The energy-scaled design serves as the basis of all following calculations.

The $\bar{\sigma}$ stability analysis mentioned previously becomes doubtful in cases of targets with very poor stability characteristics. This is because the analysis assumes a continuous inner ice layer to evaluate. For seriously perturbed implosions, however, the target shell can break apart, failing to provide the continuous interface. Such is the case for the $\alpha = 2$ design without the benefit of a stabilizing picket. The effective $\bar{\sigma}$ value for this design with the current levels of nonuniformities present on OMEGA is greater than 10 μm . As was shown in Ref. 9, the main fuel layer for this implosion was seriously perturbed and on the verge of breakup. Dramatic improvement in layer integrity was achieved, however, when a stabilizing picket was employed. The calculated $\bar{\sigma}$ for the $\alpha = 2$ with picket ($\alpha 2p$) falls close to 1 μm . With the addition of the picket it now becomes possible to evaluate $\alpha 2p$ target performance using the $\bar{\sigma}$ analysis.

Many 2-D *DRACO* simulations were run to evaluate the performance of the $\alpha 2p$ design under the influence of various levels of laser imprint, laser power imbalance, and cryogenic ice roughness. For example, we show two isodensity contours of the $\alpha 2p$ target imploded with a 1- μm inner ice roughness in Fig. 97.8(a). The image shows split contours taken at $t = 2.3$ ns (end of acceleration) and at $t = 2.7$ ns (peak neutron production). Analyzing the inner-ice-roughness spectrum at the first time yields the $\bar{\sigma}$ parameter for this run ($\bar{\sigma} = 0.52$), while the final neutron performance is determined by the core conditions at the second time (YOQ = 77%). A scan of target performance for the $\alpha 2p$ design as a function of ice roughness is shown in Fig. 97.8(b).

Such simulations provide the necessary information to develop the $\bar{\sigma}$ scaling for this design as shown in Fig. 97.9. From this graph it can be seen that the OMEGA $\alpha 2p$ design is almost as stable as the $\alpha = 4$ design. Such results allow for the confident fielding of low-adiabat direct-drive target designs on both OMEGA and the NIF. The design and testing of the laser picket required for the OMEGA $\alpha 2p$ target is already underway at LLE, and experiments should commence in mid-FY04.

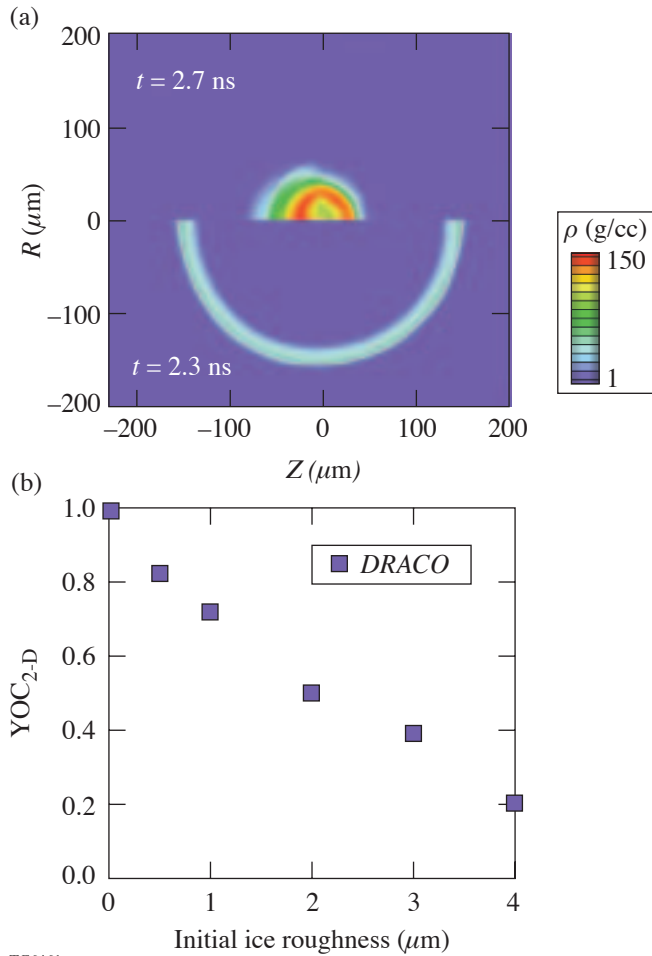


Figure 97.8 Results of a series of DRACO simulations evaluating YOC degradation due to increasing inner ice roughness. (a) Split isodensity contours drawn at $t = 2.3$ ns (end of acceleration phase) and at $t = 2.7$ ns (stagnation); (b) decay of YOC with increasing ice roughness.

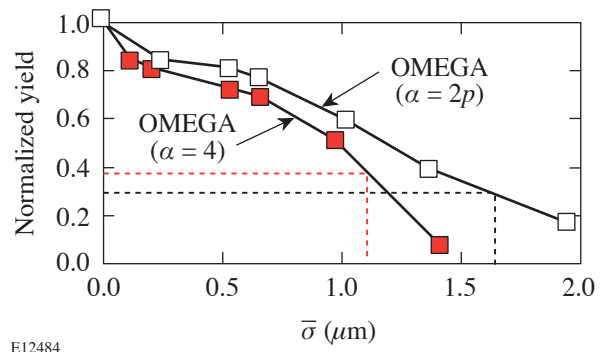


Figure 97.9 Comparison of the $\bar{\sigma}$ stability analysis for the OMEGA $\alpha = 4$ and the OMEGA $\alpha = 2p$ designs. The dashed lines indicate the predicted value of $\bar{\sigma}$ and the corresponding target performance for each of the two designs when all NIF specifications for levels of nonuniformity are applied.

Conclusion

The cryogenic implosion campaign at LLE is a staged program comprised of several concurrent efforts including the experimental validation of target performance for progressively lower fuel-adiabat target designs; the physical minimization of the interfacial cryogenic surface roughness; and ultimately the fielding and imploding of cryogenic DT targets on the OMEGA laser system. Recent advances in all three of these efforts have LLE poised to demonstrate scaled-ignition performance with DT on OMEGA by the end of FY05. In the area of target implosions, significant progress has been made with several series of cryogenic implosion experiments evaluating target performance with high-adiabat solid-D₂ and WF targets and low-adiabat solid-D₂ targets. It has been shown that there is good agreement between the experimental observables and the results of 2-D DRACO simulations for targets imploded near target chamber center. The use of adiabat shaping has led to increased stability for both the “all-DT” and wetted-foam direct-drive NIF point designs and the corresponding ignition-scaled experiments for OMEGA. Dramatic advances in cryogenic layer characterization and layering over the last year have resulted in LLE producing sub-2- μm ice layers in targets for implosion on OMEGA. The cryogenic DT fill and transfer station (FTS) is currently being qualified and will be DT-charged by the end of this fiscal year. With this system in place, full-scale layering studies of cryogenic DT ice will be undertaken, resulting in the fielding of ignition-scale cryogenic DT targets on OMEGA.

ACKNOWLEDGMENT

The authors are extremely grateful to the staff of the Laboratory for Laser Energetics for their tireless dedication to the cryogenic implosion program and the operation of the OMEGA laser system. In particular, the authors would like to acknowledge the efforts of the Cryogenic Target Fabrication Group for the production of layered and characterized capsules on a regular schedule. This work was supported by the U. S. Department of Energy Office of Inertial Confinement Fusion under Cooperative Agreement No. DE-FC03-92SF19460, the University of Rochester, and the New York State Energy Research and Development Authority. The support of the DOE does not constitute an endorsement by the DOE of the views expressed in this article.

REFERENCES

1. T. R. Boehly, D. L. Brown, R. S. Craxton, R. L. Keck, J. P. Knauer, J. H. Kelly, T. J. Kessler, S. A. Kumpan, S. J. Loucks, S. A. Letzring, F. J. Marshall, R. L. McCrory, S. F. B. Morse, W. Seka, J. M. Soures, and C. P. Verdon, *Opt. Commun.* **133**, 495 (1997).
2. W. J. Hogan, E. I. Moses, B. E. Warner, M. S. Sorem, and J. M. Soures, *Nucl. Fusion* **41**, 567 (2001).
3. P. W. McKenty, V. N. Goncharov, R. P. J. Town, S. Skupsky, R. Betti, and R. L. McCrory, *Phys. Plasmas* **8**, 2315 (2001).
4. R. Betti, K. Anderson, V. N. Goncharov, R. L. McCrory, D. D. Meyerhofer, S. Skupsky, and R. P. J. Town, *Phys. Plasmas* **9**, 2277 (2002).
5. W. K. Levedahl and J. D. Lindl, *Nucl. Fusion* **37**, 165 (1997).
6. M. C. Herrmann, M. Tabak, and J. D. Lindl, *Phys. Plasmas* **8**, 2296 (2001).
7. A. Kemp, J. Meyer-ter-Vehn, and S. Atzeni, *Phys. Rev. Lett.* **86**, 3336 (2001).
8. D. Keller, T. J. B. Collins, J. A. Delettrez, P. W. McKenty, P. B. Radha, B. Whitney, and G. A. Moses, *Bull. Am. Phys. Soc.* **44**, 37 (1999).
9. V. N. Goncharov, J. P. Knauer, P. W. McKenty, P. B. Radha, T. C. Sangster, S. Skupsky, R. Betti, R. L. McCrory, and D. D. Meyerhofer, *Phys. Plasmas* **10**, 1906 (2003).
10. T. J. Kessler, Y. Lin, J. J. Armstrong, and B. Velazquez, in *Laser Coherence Control: Technology and Applications*, edited by H. T. Powell and T. J. Kessler (SPIE, Bellingham, WA, 1993), Vol. 1870, pp. 95–104.
11. T. R. Boehly, V. A. Smalyuk, D. D. Meyerhofer, J. P. Knauer, D. K. Bradley, R. S. Craxton, M. J. Guardalben, S. Skupsky, and T. J. Kessler, *J. Appl. Phys.* **85**, 3444 (1999).
12. S. Skupsky, R. W. Short, T. Kessler, R. S. Craxton, S. Letzring, and J. M. Soures, *J. Appl. Phys.* **66**, 3456 (1989).
13. F. J. Marshall, J. A. Delettrez, R. Epstein, R. Forties, R. L. Keck, J. H. Kelly, P. W. McKenty, S. P. Regan, and L. J. Waxer, *Phys. Plasmas* **11**, 251 (2004).
14. J. Koch, Lawrence Livermore National Laboratory, private communication (2000).
15. S. Jin, *2002 Summer Research Program for High School Juniors at the University of Rochester's Laboratory for Laser Energetics*, Laboratory for Laser Energetics Report No. 329, NTIS document No. DOE/SF/19460-479 (2003). Copies may be obtained from the National Technical Information Service, Springfield, VA 22161.
16. R. Stephens, General Atomics, private communication (2003).
17. T. C. Sangster, J. A. Delettrez, R. Epstein, V. Yu. Glebov, V. N. Goncharov, D. R. Harding, J. P. Knauer, R. L. Keck, J. D. Kilkenny, S. J. Loucks, L. D. Lund, R. L. McCrory, P. W. McKenty, F. J. Marshall, D. D. Meyerhofer, S. F. B. Morse, S. P. Regan, P. B. Radha, S. Roberts, W. Seka, S. Skupsky, V. A. Smalyuk, C. Sorce, J. M. Soures, C. Stoeckl, K. Thorp, J. A. Frenje, C. K. Li, R. D. Petrasso, F. H. Séguin, K. A. Fletcher, S. Padalino, C. Freeman, N. Izumi, J. A. Koch, R. A. Lerche, M. J. Moran, T. W. Phillips, and G. J. Schmid, *Phys. Plasmas* **10**, 1937 (2003).
18. V. Yu. Glebov, D. D. Meyerhofer, C. Stoeckl, and J. D. Zuegel, *Rev. Sci. Instrum.* **72**, 824 (2001).
19. F. H. Séguin, C. K. Li, D. G. Hicks, J. A. Frenje, K. M. Green, R. D. Petrasso, J. M. Soures, D. D. Meyerhofer, V. Yu. Glebov, C. Stoeckl, P. B. Radha, S. Roberts, C. Sorce, T. C. Sangster, M. D. Cable, S. Padalino, and K. Fletcher, *Phys. Plasmas* **9**, 2725 (2002).
20. T. J. Murphy, R. E. Chrien, and K. A. Klare, *Rev. Sci. Instrum.* **68**, 610 (1997).
21. C. K. Li, F. H. Séguin, D. G. Hicks, J. A. Frenje, K. M. Green, S. Kurebayashi, R. D. Petrasso, D. D. Meyerhofer, J. M. Soures, V. Yu. Glebov, R. L. Keck, P. B. Radha, S. Roberts, W. Seka, S. Skupsky, C. Stoeckl, and T. C. Sangster, *Phys. Plasmas* **8**, 4902 (2001).
22. C. Stoeckl, V. Yu. Glebov, S. Roberts, T. C. Sangster, R. A. Lerche, R. L. Griffith, and C. Sorce, *Rev. Sci. Instrum.* **74**, 1713 (2003).
23. R. D. Petrasso, J. A. Frenje, C. K. Li, F. H. Séguin, J. R. Rygg, B. E. Schwartz, S. Kurebayashi, P. B. Radha, C. Stoeckl, J. M. Soures, J. Delettrez, V. Yu. Glebov, D. D. Meyerhofer, and T. C. Sangster, *Phys. Rev. Lett.* **90**, 095002 (2003).
24. M. C. Richardson, P. W. McKenty, F. J. Marshall, C. P. Verdon, J. M. Soures, R. L. McCrory, O. Barnouin, R. S. Craxton, J. Delettrez, R. L. Hutchison, P. A. Jaanimagi, R. Keck, T. Kessler, H. Kim, S. A. Letzring, D. M. Roback, W. Seka, S. Skupsky, B. Yaakobi, S. M. Lane, and S. Prussin, in *Laser Interaction and Related Plasma Phenomena*, edited by H. Hora and G. H. Miley (Plenum Publishing, New York, 1986), Vol. 7, pp. 421–448.
25. G. Hazak *et al.*, *Phys. Plasmas* **5**, 4357 (1998).
26. A. D. Kotelnikov and D. C. Montgomery, *Phys. Fluids* **10**, 2037 (1998).
27. A. Frank, Department of Physics and Astronomy, University of Rochester, private communication (2003).

28. C. P. Verdon, *Bull. Am. Phys. Soc.* **38**, 2010 (1993).
29. S. V. Weber *et al.*, *ICF Quarterly Report* **7**, 43, Lawrence Livermore National Laboratory, Livermore, CA, UCRL-LR-105821-97-2 (1997).
30. Laboratory for Laser Energetics LLE Review **79**, 121, NTIS document No. DOE/SF/19460-317 (1999). Copies may be obtained from the National Technical Information Service, Springfield, VA 22161.
31. V. N. Goncharov, P. McKenty, S. Skupsky, R. Betti, R. L. McCrory, and C. Cherfils-Clérouin, *Phys. Plasmas* **7**, 5118 (2000).
32. M. Tabak, *ICF Program Annual Report 1989(U)*, Lawrence Livermore National Laboratory, Livermore, CA, UCRL-LR-116901-88/80, 141 (1989) (unpublished).
33. T. J. B. Collins and S. Skupsky, *Phys. Plasmas* **9**, 275 (2002).
34. T. J. B. Collins, Laboratory for Laser Energetics, private communication (2003).
35. J. Perkins, Lawrence Livermore National Laboratory, private communication (2003).
36. A. J. Schmitt *et al.*, "Large-Scale, High-Resolution Simulations of High-Gain, Direct-Drive ICF Targets," to be published in *Physics of Plasmas*.